Journal of Molecular Medicine (2021) 99:241–255
https://doi.org/10.1007/s00109-020-02005-7

JMolMed

ORIGINAL ARTICLE

Identification of the immune gene expression signature associated with recurrence of high-grade gliomas

Adria-Jaume Roura[1] · Bartlomiej Gielniewski[1] · Paulina Pilanc[1] · Paulina Szadkowska[1] · Marta Maleszewska[1] · Sylwia K. Krol[1] · Ryszard Czepko[2] · Wojciech Kaspera[3] · Bartosz Wojtas[1] · Bozena Kaminska[1]

Received: 11 August 2020 / Revised: 26 October 2020 / Accepted: 29 October 2020 / Published online: 19 November 2020

Abstract

High-grade gliomas (HGGs), the most common and aggressive primary brain tumors in adults, inevitably recur due to incomplete surgery or resistance to therapy. Intratumoral genomic and cellular heterogeneity of HGGs contributes to therapeutic resistance, recurrence, and poor clinical outcomes. Transcriptomic profiles of HGGs at recurrence have not been investigated in detail. Using targeted sequencing of cancer-related genes and transcriptomics, we identified single nucleotide variations, small insertions and deletions, copy number aberrations (CNAs), as well as gene expression changes and pathway deregulation in 16 pairs of primary and recurrent HGGs. Most of the somatic mutations identified in primary HGGs were not detected after relapse, suggesting a subclone substitution during the tumor progression. We found a novel frameshift insertion in the *ZNF384* gene which may contribute to extracellular matrix remodeling. An inverse correlation of focal CNAs in *EGFR* and *PTEN* genes was detected. Transcriptomic analysis revealed downregulation of genes involved in messenger RNA splicing, cell cycle, and DNA repair, while genes related to interferon signaling and phosphatidylinositol (PI) metabolism are upregulated in secondary HGGs when compared to primary HGGs. In silico analysis of the tumor microenvironment identified M2 macrophages and immature dendritic cells as enriched in recurrent HGGs, suggesting a prominent immunosuppressive signature. Accumulation of those cells in recurrent HGGs was validated by immunostaining. Our findings point to a substantial transcriptomic deregulation and a pronounced infiltration of immature dendritic cells in recurrent HGG, which may impact the effectiveness of frontline immunotherapies in the GBM management.

Key messages

- Most of the somatic mutations identified in primary HGGs were not detected after relapse.
- Focal CNAs in *EGFR* and *PTEN* genes are inversely correlated in primary and recurrent HGGs.
- Transcriptomic changes and distinct immune-related signatures characterize HGG recurrence.
- Recurrent HGGs are characterized by a prominent infiltration of immature dendritic and M2 macrophages.

Keywords Recurrent high-grade glioma · Tumor microenvironment · Immune signature · Copy number aberrations · Immunohistochemistry

✉ Bartosz Wojtas
b.wojtas@nencki.edu.pl

[1] Nencki Institute of Experimental Biology, Warsaw, Poland

[2] Clinical Department of Neurosurgery, St. Raphael Hospital, Andrzej Frycz Modrzewski Krakow University, Krakow, Poland

[3] Department of Neurosurgery, Regional Hospital, Medical University of Silesia, Sosnowiec, Poland

Introduction

High-grade gliomas (HGGs) are the most common and aggressive primary brain tumors in adults. Among those, glioblastomas (GBMs) are highly heterogeneous, invasive malignant brain tumors which harbor recurrent molecular alterations disrupting pathways involved in regulation of growth, cell cycle, DNA repair, control of chromatin state, and telomere length [1]. Intratumoral heterogeneity of GBMs and the presence of

self-renewing glioma stem cells that contribute to tumor initiation, therapeutic resistance, and recurrence are major factors contributing to poor clinical outcomes of GBM patients [2]. The most frequently altered genes in GBMs are *PTEN*, *TP53*, *EGFR*, *PIK3CA*, *PIK3R1*, *NF1*, *RB1*, *IDH1*, and *PDGFRA* [3, 4]. Those alterations occur primarily by mutations, short deletions and insertions (indels), and copy number aberrations (CNAs). Genomic gains of chromosome 7 and losses of chromosome 10 represent the most common gross chromosomal abnormalities in GBMs [4]. Another common feature of GBM is the overexpression of *EGFR* in more than 50% of GBMs due to the focal amplification of its locus, which activates proliferation-related signaling and supports tumor growth [5]. Whole-genome and whole-exome sequencing of multiple regions from primary and paired recurrent GBMs has revealed genetic alterations of the p53 pathway as a primary molecular event. Divergent recurrences that share a few genetic alterations with the primary tumor likely represent a clonal expansion of cells that evolved during gliomagenesis [6].

Based on gene expression profiles, GBMs are divided into proneural, neural, classical, and mesenchymal transcriptional subtypes [7], whose prevalence changes on the basis of whether it is a primary or secondary tumor [2]. Molecular subtypes of GBMs are further defined by DNA methylation patterns [8]. Bulk tumor gene expression profiles originate not only from glioma cells but also from stromal cells, including astrocytes, endothelial cells, and infiltrating immune cells of the innate and adaptive immune systems. GBMs are known as "immunologically cold" tumors due to severe immunosuppression which facilitates disease progression and limits successes of immunotherapy [9]. Glioma-infiltrating microglia and bone marrow–derived macrophages, which are the predominant immune cells in GBMs, contribute to tumor invasion and create an immunosuppressive milieu [10].

Despite a significant progress in understanding alterations in glioma genomics and the resulting deregulation of transcription, there is still lack of knowledge regarding the molecular deregulation during HGG progression and recurrence. A deeper evaluation of genomic and transcriptomic variations between primary and recurrent malignant gliomas may expand our knowledge on the molecular deregulation during HGG progression and at the recurrence. Such efforts are undertaken by the GLASS (The Glioma Longitudinal Analysis) Consortium [11] focused on molecular profiling of tumor specimens acquired at multiple time points along the course of glioma progression (https://www.glass-consortium). In this study, driven by a similar rationale, we performed targeted sequencing of cancer-related genes and RNA sequencing of 16 primary and recurrent HGG pairs to visualize comparative patterns of genomic alterations and transcriptional profiles. From RNA-Seq data obtained from bulk tumors, we extracted characteristics of immune subsets of HGGs and subsequently inferred computational changes in the cellular components of HGGs post recurrence. We identified and validated an immune gene expression signature, which reflects immunosuppressive mechanisms within the tumor microenvironment.

Materials and methods

Sample collection, genomic DNA, and RNA extraction

In total, we collected 35 fresh frozen glioma samples, representing grade III and IV HGGs (according to World Health Organization (WHO) classification) from the neurosurgery clinics of the following hospitals: Clinical Department of Neurosurgery St. Raphael Hospital, Andrzej Frycz Modrzewski Krakow University, Krakow, Poland; Regional Hospital, Medical University of Silesia, Sosnowiec, Poland; and Mazovian Brodno Hospital, Warsaw, Poland (Table 1). All patients signed an informed consent for use of their biological material for research purposes. The cohort contains 14 pairs of GBMs and 2 anaplastic astrocytomas (WHO grade III). Most of the patients were treated by the standard Stupp protocol, including surgery followed by radiotherapy plus concomitant and adjuvant temozolomide (TMZ). In this cohort, 16 samples were primary and 19 recurrent paired tumors; 2 cases were patients who underwent 2rd and 3rd resections. Blood samples were collected from each patient to identify the somatic status of single nucleotide polymorphisms (SNPs), indels, and CNAs. Total DNA, RNA, and protein from collected glioma tissue samples were extracted using TRI Reagent (Sigma-Aldrich, cat no. T9424-100ML), following the manufacturer's protocol. DNA was additionally purified by a phenol–chloroform extraction and precipitated by ethanol. Briefly, isolated DNA was incubated with proteinase K (600 μg/ml) to remove protein contamination and an equal volume of phenol–chloroform–isoamyl alcohol mixture was added. After centrifugation, the top aqueous phase was carefully transferred to a new tube, extracted with an equal volume of chloroform, and centrifuged; 5 M NaCl was added to the top aqueous phase; DNA was precipitated with 2 volumes of 100% ethanol. After centrifugation, the DNA pellet was washed with 70% ethanol and dried at room temperature, followed by resuspension in MQ water and frozen at − 20 °C. The isolated DNA was used for targeted exome sequencing and RNA for RNA-Seq, both procedures described in the following sections (Suppl. Fig. S1A).

Panel design, genomic and transcriptomic library preparation, and next generation sequencing

We designed a target enrichment DNA sequencing panel, including 700 cancer-related genes comprising the exonic regions. The target region spanning 7 MB (1×10^6 bp) covered cancer-related sites with a strong emphasis on genes coding

Table 1 Summary of clinical characteristics of patients in this study

Patient's ID	Diagnosis[a]	Age	Sex	Localization[b]	Type	Surv.[c]	Vars.[d]	Therapy[e]
PG1	AA	26	F	Frontalis dex	Primary	46	16	None
R1G1	AA	26	F	Frontalis dex	Recurrent	46	19	None
R2G1	AA	26	F	Frontalis dex	Recurrent	46	23	None
PG2	GBM	60	F	Frontal dex	Primary	14	78	R, CTX, DEX
R1G2	GBM	60	F	Frontal dex	Recurrent	14	15	R, CTX, DEX
PG3	GBM	55	F	Frontal lobe	Primary	16	39	R, DEX
R1G3	GBM	56	F	Frontal lobe	Recurrent	16	42	R, DEX
PG4	GBM	64	M	Parietal dex	Primary	12	35	R, CTX, DEX
R1G4	GBM	64	M	Temporal dex	Recurrent	12	13	R, CTX, DEX
PG5	GBM	59	M	Parieto-occipital sin	Primary	22	11	None
R1G5	GBM	59	M	Parieto-occipital sin	Recurrent	22	69	None
R2G5	GBM	59	M	Parieto-occipital sin	Recurrent	22	7	None
R3G5	GBM	59	M	Parieto-occipital sin	Recurrent	22	35	None
PG6	GBM	62	F	Temporal sin	Primary	10	33	R, CTX, DEX
R1G6	GBM	62	F	Temporal sin	Recurrent	10	11	R, CTX, DEX
PG7	GBM	34	F	Parietal dex	Primary	23	12	R, CTX, DEX
R1G7	GBM	34	F	Parietal dex	Recurrent	23	19	R, CTX, DEX
PG8	GBM	50	M	Temporal sin	Primary	13	16	R, CTX, DEX
R1G8	GBM	50	M	Temporal sin	Recurrent	13	38	R, CTX, DEX
PG9	AOD	43	F	Frontal sin	Primary	23	5	R, CTX, DEX
R1G9	AOD	43	F	Frontal sin	Recurrent	23	5	R, CTX, DEX
PG10	GBM	60	M	Temporal dex	Primary	16	16	R, CTX, DEX
R1G10	GBM	60	M	Temporal dex	Recurrent	16	13	R, CTX, DEX
PG11	GBM	44	M	Parietotemporal sin	Primary	19	11	R, CTX, DEX
R1G11	GBM	44	M	Parietotemporal sin	Recurrent	19	6	R, CTX, DEX
PG12	GBM	47	F	Temporal sin	Primary	26	11	R, CTX, DEX
R1G12	GBM	47	F	Temporal sin	Recurrent	26	11	R, CTX, DEX
PG13	GBM	71	F	Temporalis dex	Primary	16	15	R, CTX, DEX
R1G13	GBM	71	F	temporalis dex	Recurrent	16	19	R, CTX, DEX
PG14	GBM	70	F	Frontal dex	Primary	8	28	R, CTX, DEX
R1G14	GBM	70	F	Frontal dex	Recurrent	8	22	R, CTX, DEX
PG15	GBM	44	F	Temporal sin	Primary	14	6	R, CTX, DEX
R1G15	GBM	44	F	Temporal sin	Recurrent	14	11	R, CTX, DEX
PG16	GBM	77	F	Parietal dex	Primary	5	19	R, DEX
R1G16	GBM	77	F	Parietal dex	Recurrent	5	17	R, DEX

[a] High-grade glioma type where GBM indicates glioblastoma; AA indicates anaplastic astrocytoma, and AOD indicates anaplastic oligodendroglioma

[b] Tumor localization where *sin* indicates *sinister* (left) and *dex* indicates *dexter* (right)

[c] Survival time from primary diagnosis

[d] High-confidence somatic variants

[e] Adjuvant therapy where *R* indicates radiotherapy, *CTX* indicates chemotherapy, and *DEX* indicates dexamethasone

for epigenetic regulators (histone modifiers, chromatin modelers, histone chaperones). Targeted exome sequencing was performed as previously described [12]. RNA-Seq was performed using the KAPA Stranded mRNA-Seq Kit (Illumina® Platforms), required for poly(A) messenger RNA (mRNA) capture and construction of stranded mRNA-Seq libraries. Both DNA sequencing and RNA sequencing were performed using the Illumina HiSeq® 1500 system.

Quality and integrity of total RNA was assessed with an Agilent 2100 Bioanalyzer using an RNA 6000 Nano Kit (Agilent Technologies, Ltd.). Strand-specific polyA-enriched RNA libraries were prepared using the KAPA Stranded

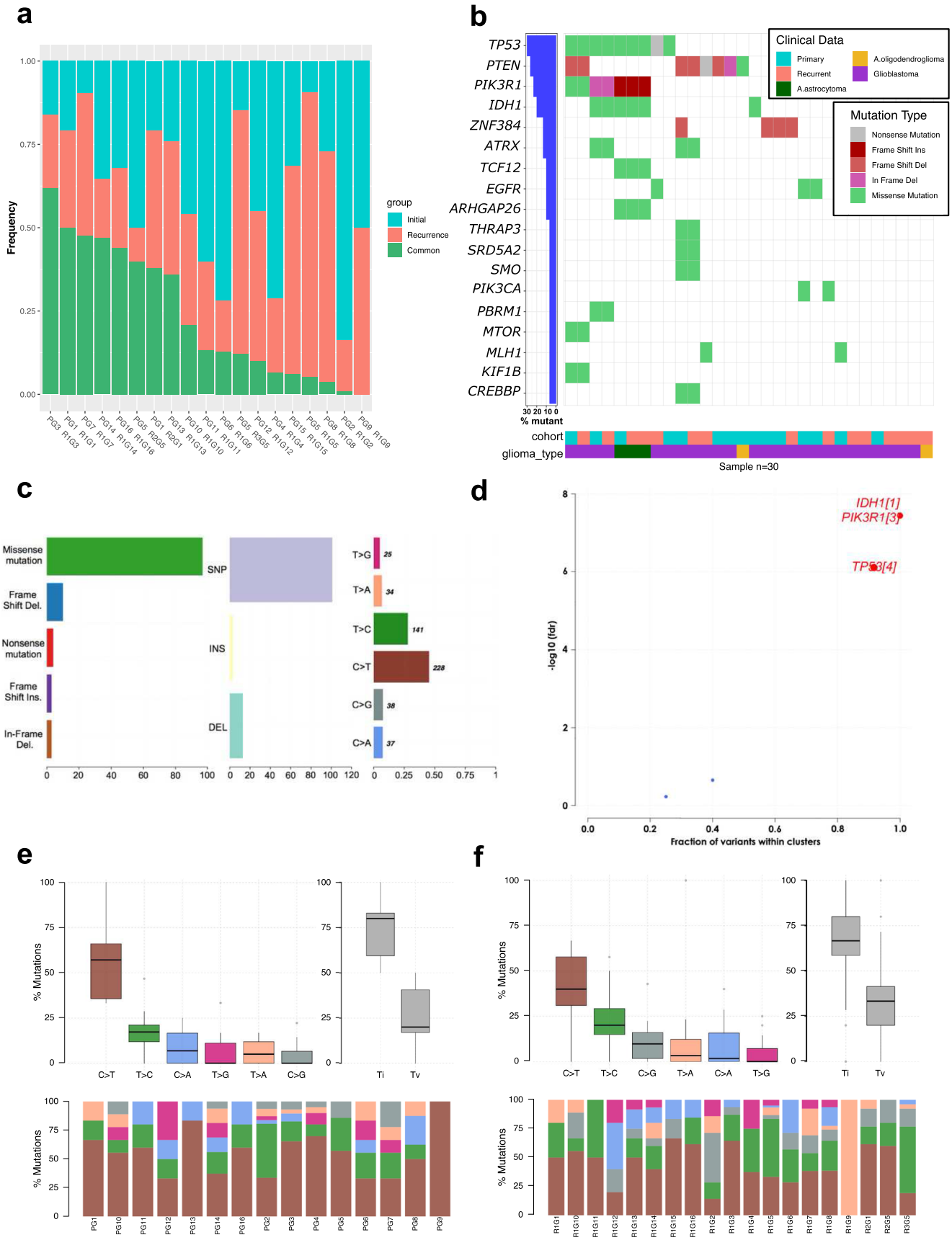
a
Frequency
group
Initial
Recurrence
Common
b
TP53
PTEN
PIK3R1
IDH1
ZNF384
ATRX
TCF12
EGFR
ARHGAP26
THRAP3
SRD5A2
SMO
PIK3CA
PBRM1
MTOR
MLH1
KIF1B
CREBBP
% mutant
cohort
glioma_type
Sample n=30
Clinical Data
Primary
Recurrent
A.astrocytoma
A.oligodendroglioma
Glioblastoma
Mutation Type
Nonsense Mutation
Frame Shift Ins
Frame Shift Del
In Frame Del
Missense Mutation
c
Missense mutation
Frame Shift Del.
Nonsense mutation
Frame Shift Ins.
In-Frame Del.
SNP
INS
DEL
T>G
T>A
T>C
C>T
C>G
C>A
d
IDH1[1]
PIK3R1[3]
TP53[4]
-log10 (fdr)
Fraction of variants within clusters
e
% Mutations
C>T
T>C
C>A
T>G
T>A
C>G
Ti
Tv
f
% Mutations
C>T
T>C
C>G
T>A
C>A
T>G
Ti
Tv

◀ **Fig. 1** Mutational landscape of high-grade gliomas. **a** Frequency of high-confidence non-synonymous somatic mutations (VAF > 15%, normal VAF < 5%, and a somatic *p* value of < 0.03) occurring exclusively in initial HGGs (cyan), exclusively in recurrent HGGs (salmon), and in both (green). **b** Mutation waterfall plot showing somatic mutation types and status found in at least 2 samples and with SIFT values < 0.05 in the case of SNP. Types of somatic alterations are ordered by the frequency of the occurrence in studied cohort. **c** Summary plot indicating the most common type of somatic mutations and nucleotide substitution in all cohorts. **d** Positional clustering showing cancer-driver genes from the cohort, using OncodriveCLUST algorithm and corrected by FDR < 0.1. Numbers enclosed in square brackets represent the number of clusters found per gene, and dots in red correspond to statistically significant clusters. **e**, **f** Boxplots show the distribution of different nucleotide conversions across primary and recurrent HGG samples and the overall transition and transversion frequencies

mRNA Sample Preparation Kit according to the manufacturer's protocol (Kapa Biosystems, MA, USA). Briefly, mRNA molecules were enriched from 500 ng of total RNA using poly-T oligo-attached magnetic beads (Kapa Biosystems, MA, USA). Obtained mRNA was fragmented, and first-strand complementary DNA (cDNA) was synthesized using a reverse transcriptase. Second cDNA synthesis was performed to generate double-stranded cDNA (dsDNA). Adenosines were added to the 3′ ends of dsDNA, and adapters were ligated (adapters from NEB, Ipswich, MA, USA). Following adapter ligation, uracil in a loop structure of adapter was digested by USER Enzyme from NEB (Ipswich, MA, USA). Adapters containing DNA fragments were amplified by PCR using NEB starters (Ipswich MA, USA). Library evaluation was done with the Agilent 2100 Bioanalyzer using the Agilent DNA High Sensitivity chip (Agilent Technologies, Ltd.). Mean library size was 300 bp. Libraries were quantified using a Quantus Fluorometer and QuantiFluor dsDNA System (Promega, Madison, Wisconsin, USA). Libraries were run in the rapid run flow cell and were paired-end sequenced (2 × 76 bp) on HiSeq 1500 (Illumina, San Diego, CA, 92122 USA).

Genomic analysis and detection of copy number aberrations

Read trimming was applied to FASTQ files using Trimmomatic [13] (version 0.36) with default parameter values and paired-end mode in order to remove Illumina-specific adapters, low-quality 5′ and 3′ bases, and short reads. DNA sequencing reads were aligned to a reference genome sequence (hg38) using NextGenMap [14] (version 0.5.2), with default parameters and "strata" variables. Mark and removal of duplicates was performed by Picard Tools [15] (version 2.17.1). Only properly oriented and uniquely mapped reads were considered for further analysis. For somatic calls, a minimum coverage of 10 reads was established for both normal and tumor samples. Additionally, variants with strand bias were discarded; damaging coding variants with predicted Sorting Intolerant From Tolerant (SIFT) values (SIFT < 0.05) were considered for further analysis. Finally, ProcessSomatic method from VarScan 2 [16] was applied to extract high-confidence somatic calls based on variant allele frequency (VAF) and Fisher's exact test *p* value (VAF > 15%, normal VAF < 5%, and a somatic *p* value of < 0.03). The final subset of variants was annotated with Annovar [17] (2017Jul version) employing the latest database versions (refGene, clinvar, cosmic, avsnp150, and dbnsfp30a). In parallel, OncodriveCLUST algorithm was used to identify genes whose mutations cluster in large spatial hotspots that could provide an adaptive advantage to cancer cells [18].

In order to infer relative changes in copy number alterations in HGGs, we first computed the somatic CNAs using data from matched tumor-normal pairs, followed by the application of the Circular Binary Segmentation (CBS) algorithm. Samtools (version 1.5) and VarScan 2 (version 2.4.3) were used to compute the copy number variation (CNV). Copynumber and copycaller were used with default parameters but considering the normal/tumor input data ratio.

RNA splicing and transcriptomic analysis

We evaluated the complete novel splicing events (both donor and acceptor sites of splicing are not in existing transcriptome databases) in HGGs using RNA-Seq data. RSeQC [19] (version 2.6.5) was used to detect splice junctions. RNA-Seq mapped reads were summarized to genes and counted using featureCounts [20] software (version 1.5.3).

Concerning the transcriptomic analysis, Trimmomatic (version 0.36) was used with default parameters. RNA sequencing reads were aligned to a reference genome sequence (hg38) using STAR aligner [21] (version 2.6) enabling the twopassMode Basic option. Read duplicates were marked with Picard Tools (version 2.17.1). Resulting RNA-Seq–mapped reads were summarized and counted by genes using featureCounts software (version 1.5.3), in paired and reverse stranded mode. Pre-filtering low-count genes was performed, followed by an analysis of differentially expressed genes with DESeq2 [22] (version 3.7), using a multi-factor design which included the paired sample status (recurrent/primary) to fit an individual baseline for each patient (Suppl. Table 1). Moreover, a Cook's distance cutoff of 0.5 was imposed to detect outliers in the cohort. Concurrently, raw counts were normalized using a variance stabilizing transformation to better estimate gene expression differences among samples or conditions.

Tumor microenvironment and cell enrichment

In order to understand changes in the tumor microenvironment during HGG progression, we performed an in silico

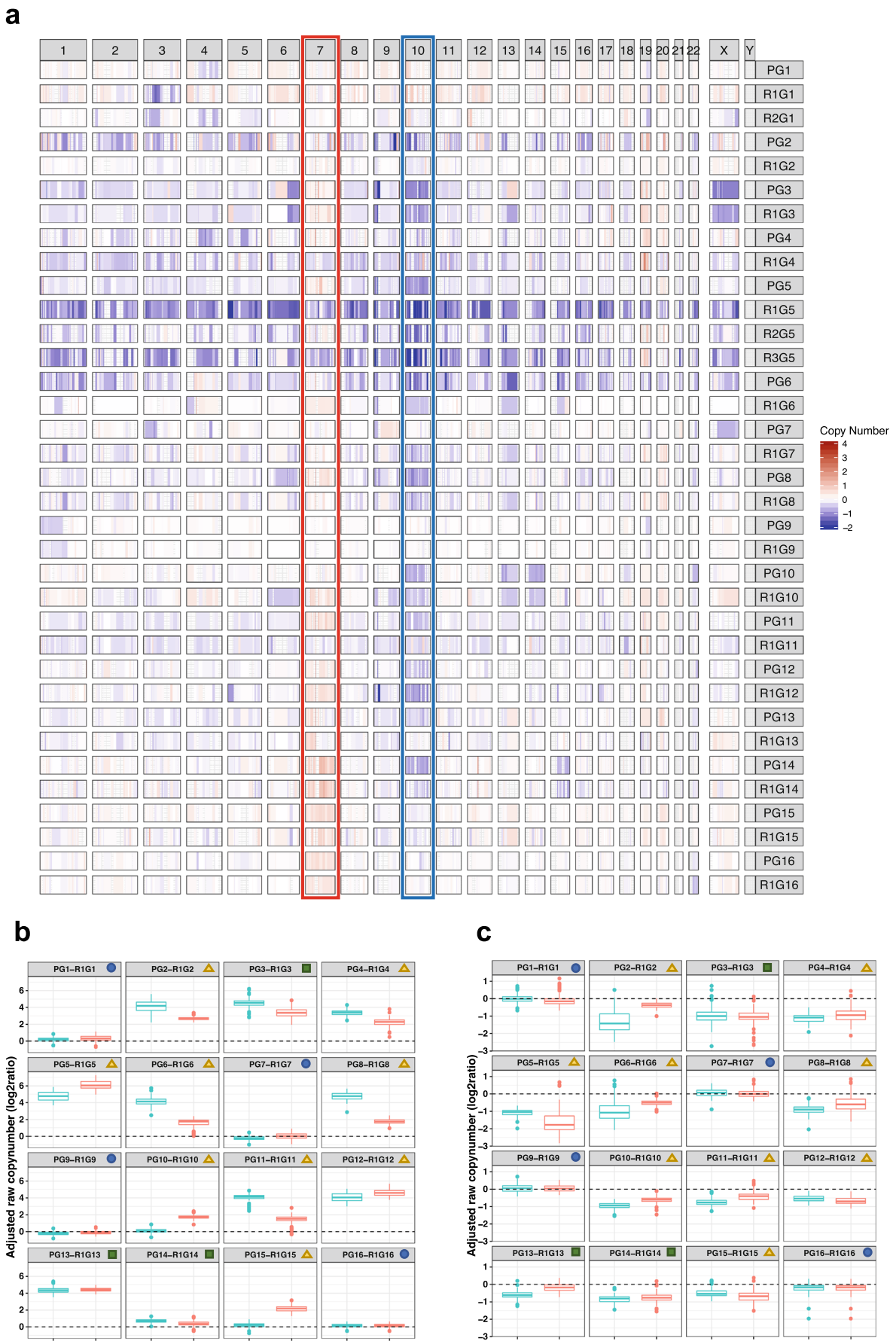
a
1 2 3 4 5 6 7 8 9 10 11 12 13 14 15 16 17 18 19 20 21 22 X Y
PG1
R1G1
R2G1
PG2
R1G2
PG3
R1G3
PG4
R1G4
PG5
R1G5
R2G5
R3G5
PG6
R1G6
PG7
R1G7
PG8
R1G8
PG9
R1G9
PG10
R1G10
PG11
R1G11
PG12
R1G12
PG13
R1G13
PG14
R1G14
PG15
R1G15
PG16
R1G16
Copy Number
4
3
2
1
0
−1
−2
b
PG1–R1G1
PG2–R1G2
PG3–R1G3
PG4–R1G4
PG5–R1G5
PG6–R1G6
PG7–R1G7
PG8–R1G8
PG9–R1G9
PG10–R1G10
PG11–R1G11
PG12–R1G12
PG13–R1G13
PG14–R1G14
PG15–R1G15
PG16–R1G16
Adjusted raw copynumber (log2ratio)
c
PG1–R1G1
PG2–R1G2
PG3–R1G3
PG4–R1G4
PG5–R1G5
PG6–R1G6
PG7–R1G7
PG8–R1G8
PG9–R1G9
PG10–R1G10
PG11–R1G11
PG12–R1G12
PG13–R1G13
PG14–R1G14
PG15–R1G15
PG16–R1G16
Adjusted raw copynumber (log2ratio)

◀ **Fig. 2** Copy number aberrations in progression of HGGs. **a** Segments of CNAs at a cohort level with rows denoting individual patients, where *P* indicates primary tumor and *R* represents recurrent tumor. UCSC hg38 genome was used to determine the chromosomal coordinates which are represented in columns by the corresponding number. CNA calling was performed using circular binary segmentation (CBS) algorithm for segmentation, and single-point outliers were smoothened before the analysis. Focal copy number aberrations of **b** *EGFR* and **c** *PTEN* are represented by the adjusted log ratio between blood DNA (reference) and tumor DNA, shown in primary (teal)–recurrent (red) paired boxplots. Header: top-right-corner blue icons indicate no focal copy number aberrations, top-right-corner yellow triangle indicates inversely correlated *EGFR* and *PTEN* focal CNAs, and top-right-corner green squares indicate no correlation

cell-type enrichment analysis with an xCell [23] webtool, using the 64 immune and stroma signature set. Weak signatures were filtered out for further analysis. In an effort to validate main xCell findings, we applied an in silico marker gene-based approach, MCP-counter [24], and three deconvolution methods, CIBERSORT [25], quanTIseq [26], and TIMER [27] to better infer the cellular composition of HGG samples using bulk gene expression data.

Validation of findings using immunohistochemistry and immunofluorescence

Tumor slides were deparaffinized and hydrated. Antigen retrieval was performed using pH 6 citrate antigen retrieval solution (Dako), followed by 30 min of 10% peroxidase and blocking solution (3% NHS) for 1 h at room temperature. A detection system (Dako) was used according to the manufacturer's instructions, followed by staining with hematoxylin. The following immunohistochemistry (IHC) antibodies were used: human CD163 (Abcam ab87099, 1:1000) and CD83 (Abcam 205343, 1:100). Immunofluorescence (IF) staining was performed as follows: The slides were dried at room temperature for 1.5 h after being transferred from the − 80 °C storage. The slides were rinsed thrice in PBS, 5 min each for rehydration, and were then blocked with 10% normal serum (donkey) made in 0.1% Triton X-100 (Tx100)/PBS for 2 h at room temperature. The primary antibodies were diluted according to the manufacturer's instructions in 3% serum in PBS (+ Tx100) and incubated overnight at 4 °C. Primary antibody was removed, and the slides were washed thrice for 5 min each with PBS, followed by incubation with respective secondary antibodies conjugated with the fluorophore, Alexa Fluor® 488 donkey anti-mouse IgG (Invitrogen A21202). The nuclei were stained with DAPI, followed by mounting of the cover slip with antifade fluorescent mounting medium (Dako, USA). Immunofluorescence quantification was performed with ImageJ; all cells in different 10 fields were counted, for each patient, and the percentage of those cells was calculated.

Results

Somatic mutational landscape and copy number aberrations in primary and recurrent high-grade gliomas

Both primary and recurrent tumor samples harbored an average of 20 high-confidence somatic mutations (Table 1). We sought to estimate how many of these mutations were maintained after the tumor relapse in 16 pairs of HGGs. Comparison of somatic mutations found in the primary and recurrent tumors shows that in most of the patients (14/16, 87.5%), a number of somatic variants unique to the primary or the recurrent tumor sample were higher than those shared between the two tumor samples (Fig. 1a). This suggests a subclone re-emergence in the course of tumor progression, a neutral evolution, or a polyclonal re-emergence [28].

In the genomic somatic analysis, in which non-synonymous mutations that could directly affect the protein structure were considered, we found *TP53* (26%), *PTEN* (23%), *PIK3R1* (20%), and *IDH1* (17%) as the most frequently altered genes in both primary and recurrent HGGs (Suppl. Fig. S1B). Other less frequently mutated genes in the cohort were *ATRX* (11%), *EGFR* (11%), and *PIK3CA* (11%), which is in agreement with other studies [3, 29, 30]. Interestingly, in four HGG samples, we identified a frameshift mutation in the *ZNF384* gene (Fig. 1b). The *ZNF384* gene encodes a C2H2-type zinc finger protein and functions as a transcription factor that regulates the extracellular matrix genes [31]. Although the detected somatic alteration is located outside any protein domain (Suppl. Fig. S1C), this mutation may affect the protein stability. Moreover, the identified *ZNF384* in-frame deletion in HGG is also described in other cancer types in the Catalogue of Somatic Mutations in Cancer (COSMIC) (Suppl. Table 2).

In general, the most frequent variant type in the cohort was a missense mutation where a cytosine (C) was substituted by a thymine (T) (Fig. 1c). This could be a result of TMZ treatment, as this drug is known to induce a disproportionate number of C > T transitions in recurrent gliomas [32]. Additionally, we found that high expression of *ZNF384* inversely correlates with survival in the TCGA-GBM/LGG dataset (Suppl. Fig. S1D).

We then used the OncodriveCLUST algorithm to identify spatial clustering hotspots that could provide an adaptive advantage to cancer cells and, consequently, positive selection during the clonal tumor evolution [18]. Results demonstrated that *TP53*, *IDH1*, and *PIK3R1* are the most frequently mutated genes, harboring significantly clustered mutations corresponding to specific protein regions (Fig. 1d). The same analysis performed on primary and recurrent HGG samples as independent cohorts revealed *ZNF384* as a potential novel candidate driver gene in the primary HGG cohort, as the specific mutation clustering was detected only in the primary tumors (Suppl. Fig. S2A). Gene hotspots in the recurrent

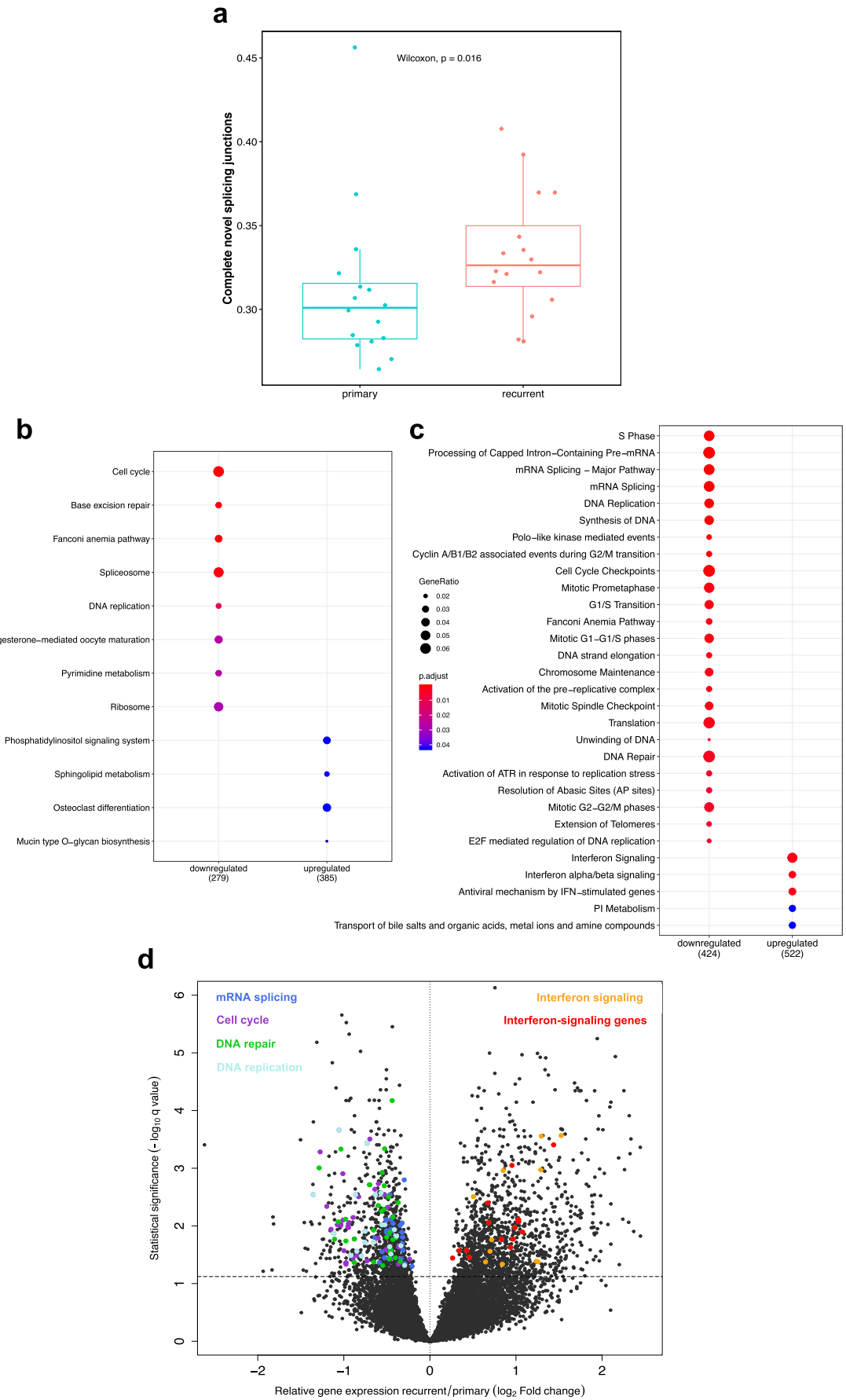
a
Wilcoxon, p = 0.016
Complete novel splicing junctions
0.45
0.40
0.35
0.30
primary
recurrent
b
Cell cycle
Base excision repair
Fanconi anemia pathway
Spliceosome
DNA replication
Progesterone−mediated oocyte maturation
Pyrimidine metabolism
Ribosome
Phosphatidylinositol signaling system
Sphingolipid metabolism
Osteoclast differentiation
Mucin type O−glycan biosynthesis
downregulated (279)
upregulated (385)
c
S Phase
Processing of Capped Intron−Containing Pre−mRNA
mRNA Splicing − Major Pathway
mRNA Splicing
DNA Replication
Synthesis of DNA
Polo−like kinase mediated events
Cyclin A/B1/B2 associated events during G2/M transition
Cell Cycle Checkpoints
Mitotic Prometaphase
G1/S Transition
Fanconi Anemia Pathway
Mitotic G1−G1/S phases
DNA strand elongation
Chromosome Maintenance
Activation of the pre−replicative complex
Mitotic Spindle Checkpoint
Translation
Unwinding of DNA
DNA Repair
Activation of ATR in response to replication stress
Resolution of Abasic Sites (AP sites)
Mitotic G2−G2/M phases
Extension of Telomeres
E2F mediated regulation of DNA replication
Interferon Signaling
Interferon alpha/beta signaling
Antiviral mechanism by IFN−stimulated genes
PI Metabolism
Transport of bile salts and organic acids, metal ions and amine compounds
GeneRatio
0.02
0.03
0.04
0.05
0.06
p.adjust
0.01
0.02
0.03
0.04
downregulated (424)
upregulated (522)
d
mRNA splicing
Cell cycle
DNA repair
DNA replication
Interferon signaling
Interferon-signaling genes
Statistical significance (- log10 q value)
Relative gene expression recurrent/primary (log2 Fold change)

◀ **Fig. 3** Transcriptomic alterations and detection of differentially expressed genes. **a** Complete novel splicing junction alterations in primary and recurrent HGGs were detected using a reference gene model from RefSeq (hg38). Data shown represent the arcsin transformation, and the *p* value was calculated using the Wilcoxon signed-rank test. **b**, **c** KEGG and Reactome analysis of differentially expressed genes showing regulatory pathways in recurrent samples. Raw counts were pre-filtered (> 10 reads within the cohort), Cook's distance cutoff of 0.5 was imposed, and the Benjamini–Hochberg (BH) procedure was used to correct for multiple testing. **d** Volcano plot shows downregulated and upregulated genes ($\log_2$ fold change < 0 and $\log_2$ fold change > 0, respectively, and BH FDR correction $p < 0.05$) in recurrent HGGs relative to primary HGGs. Each dot above the dashed line (corresponding to the *q* value = 0.05) represents one significantly altered gene. Genes from selected functional KEGG and Reactome categories are marked in different colors, as indicated

cohort were similar to those in the entire cohort (Suppl. Fig. S2B). Concurrently, we inspected a number of transitions (Ti) and transversions (Tv) in both primary and recurrent HGG groups (Fig. 1e, f). Tv are more likely to alter the amino acid sequence of proteins due to larger changes in the shape of the DNA backbone with a bigger impact on regulatory DNA [33]. We noticed that the ratio of Ti/Tv slightly decreases in recurrent HGG; however, this change was negligible. We computed the somatic CNAs using data from matched tumor-normal pairs, and we identified the presence of repeated and consistent CNAs, mainly on chromosomes 7 and 10 (Fig. 2a), indicating frequent DNA duplications or deletions in these areas, which is in line with previous findings [8]. Amplification of *EGFR* was a common trait in most of the HGGs (75%, 12/16), both primary and recurrent (Fig. 2b). This amplification was maintained after recurrence, with varying intensities in the patients. Further, we observed a lack of *PTEN* deletion in several HGGs after recurrence (Fig. 2c). Strikingly, the copy number of *EGFR* and *PTEN* was inversely correlated; in tumors with higher levels of *EGFR* amplification, a higher level of *PTEN* deletion was found in both primary and recurrent cohorts (Fig. 2c, Suppl. Fig. S3).

Deregulation of splicing and gross changes in transcription characterize recurrent HGGs

We employed the RSeQC package to comprehensively evaluate the RNA-Seq data, test sequence quality, GC, PCR and nucleotide composition bias, sequencing depth, strand specificity, coverage uniformity, and read genomic distribution. We found no significant differences in these parameters (data not shown). However, we detected an increase in a proportion of complete novel splicing events in recurrent HGGs in this analysis (Fig. 3a), suggesting higher transcriptomic variability post recurrence. This increase in alternative splicing could produce transcriptomic instability, novel transcripts, and potentially non-functional proteins.

Gene Ontology functional enrichment and Kyoto Encyclopedia of Genes and Genomes (KEGG) pathway analyses were performed on the differentially expressed genes. Analyses of KEGG pathways revealed a large group of differentially expressed genes involved in interferon (IFN) signaling, IFN stimulation, phosphatidylinositol (PI) signaling, and sphingolipid metabolism that were upregulated in recurrent HGGs. Genes involved in cell cycle, base excision repair, DNA replication, and spliceosome were downregulated in recurrent HGGs (Fig. 3b, Suppl. Fig. S4). The observed reduction of spliceosome-related genes is in agreement with the observed increases in novel splicing events, because spliceosomes are crucial complexes for the maturation of the transcribed pre-mRNA [34]. Using the Reactome database, we demonstrated upregulation in pathways related to interferon signaling, IFN-stimulated genes, and PI metabolism in recurrent HGGs. On the other hand, pathways downregulated in recurrent HGGs were linked to mRNA splicing, DNA synthesis, repair, and replication (Fig. 3c, d). These findings support the notion that recurrent HGGs are associated with upregulation of pathways implicated in the immune response. Moreover, the results of the analyses suggest that in recurrent HGGs, a vast number of differentially expressed genes (704) coding for cell cycle, DNA repair, and splicing proteins are downregulated. This downregulation may lead to deregulation of cell cycle phases, chromosome maintenance, cell cycle checkpoints, and pre-mRNA processing (Suppl. Fig. S4–S5).

Increased expression of genes related to the immune response and markers of M2 macrophages/immature dendritic cells in the HGG microenvironment

Among differentially expressed genes in recurrent HGGs, we found many genes that are related to the immune response. xCell cell enrichment scores revealed remarkable differences between primary and recurrent HGG, primarily in abundance of immune cells such as M2 (pro-tumorigenic) macrophages, immature dendritic cells (iDCs), and T helper cells (Th1), but also in megakaryocyte–erythroid progenitor (MEP) cells and pro-B cells (Fig. 4a), among others. The iDC signature was more prominent in recurrent HGGs. CIBERSORT and quanTIseq approaches (Suppl. Fig. S6A-B) confirmed the increase of M2 macrophages in the recurrent state, while MCP-counter and TIMER approaches (Suppl. Fig. S6C-D) showed higher myeloid dendritic cell enrichment scores in recurrent HGGs. On the other hand, cell enrichment scores in monocytes and M0 macrophages were higher in primary HGGs.

Expression of genes coding for numerous immunoglobulins (Igs) and immunoglobulin-related molecules was more

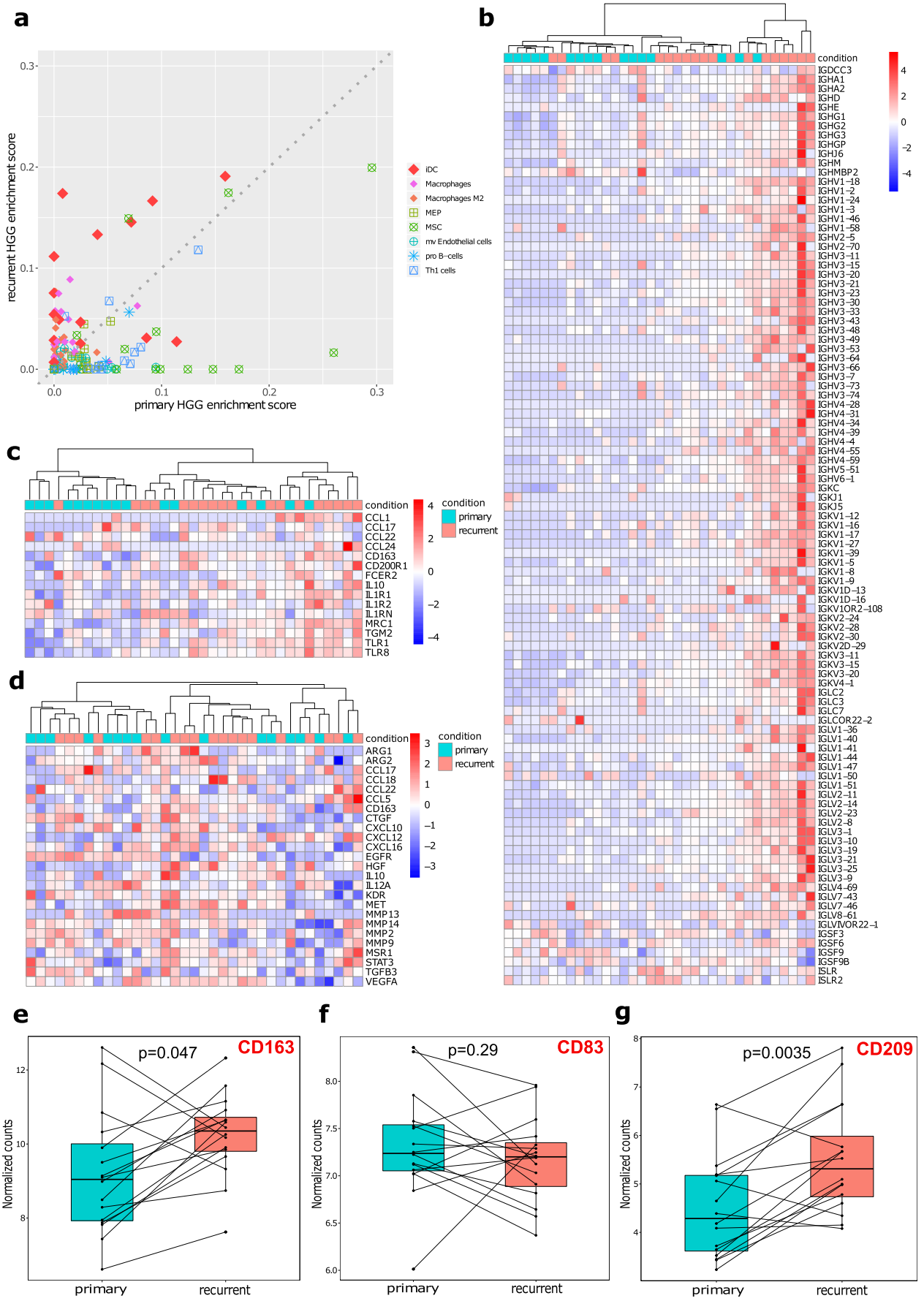
a
recurrent HGG enrichment score
primary HGG enrichment score
iDC
Macrophages
Macrophages M2
MEP
MSC
mv Endothelial cells
pro B−cells
Th1 cells
b
condition
c
condition
primary
recurrent
CCL1
CCL17
CCL22
CCL24
CD163
CD200R1
FCER2
IL10
IL1R1
IL1R2
IL1RN
MRC1
TGM2
TLR1
TLR8
d
ARG1
ARG2
CCL17
CCL18
CCL22
CCL5
CD163
CTGF
CXCL10
CXCL12
CXCL16
EGFR
HGF
IL10
IL12A
KDR
MET
MMP13
MMP14
MMP2
MMP9
MSR1
STAT3
TGFB3
VEGFA
e
p=0.047
CD163
Normalized counts
primary
recurrent
f
p=0.29
CD83
g
p=0.0035
CD209

◀ **Fig. 4** Immune cell heterogeneity in primary and recurrent HGGs. **a** Cell type enrichment analysis from normalized gene expression data using a 64-immune and stroma signature set shows significant differences in enrichment scores between primary and recurrent cohorts. iDC, immature dendritic cells; MEP, megakaryocyte–erythroid progenitor cells; MSC, mesenchymal stem cells. *p* values were calculated using the Wilcoxon signed-rank test, and the most significant signatures are presented. **b**–**d** Heat maps show mRNA expression of **b** immunoglobulins and immunoglobulin-related molecules, **c** expression levels of markers of M2 macrophages, and **d** glioma-associated macrophages. Raw count values were normalized using a variance-stabilizing transformation method from DESeq2, and samples were clustered using Ward's method. **e**–**g** Box plots representing markers selected for immunohistochemistry: CD163, CD83, and CD209, respectively

prominent in recurrent HGGs (Fig. 4b); however, the levels of expression did not pass the pre-filtering criteria in the differential gene expression analysis. Expression of markers of tumor-associated M2 macrophages [35] was higher in recurrent HGGs, as depicted in the hierarchical clustering (Fig. 4c), showing the importance of pro-tumorigenic macrophages in glioma progression. Glioma-associated microglia/macrophages (GAMs) are attracted and reprogramed by glioma cells into invasion-supporting immunosuppressive cells [12]. Accordingly, we found a pronounced expression level of GAM biomarkers in recurrent HGGs (Fig. 4d), indicating a higher abundance of these immune cells. We focused on mRNA levels of specific differentially expressed markers for M2 macrophages, iDC and DC in the dataset (Fig. 4e–g); we observed an increase in mRNA levels for markers of iDC and M2 macrophages.

To validate the above results, we used an antibody recognizing the scavenger receptor cysteine-rich (SRCR/CD163) for detection of M2 macrophages, antibody against dendritic cell-specific ICAM-3-grabbing non-integrin 1 (DC-SIGN/CD209) for the detection of mature dendritic cells (mDCs) and immunosuppressive cells, and anti-CD83 antibody for detecting mDCs. We found an increased number of $CD209^+$ cells in recurrent GBMs when compared to primary GBMs (Fig. 5a). Quantification of $CD209^+$ cells confirmed the observed changes (Fig. 5b). Staining with an antibody against mDCs showed no differences between primary and recurrent HGGs. We also detected a higher number of $CD163^+$ cells in the brain parenchyma and perivascular spaces in recurrent GBMs when compared to primary ones.

Discussion

Understanding genomic and transcriptomic changes underlying HGG progression and recurrence in the context of changes in the tumor microenvironment provides essential insights into the evolution of malignant gliomas and facilitates designing a better treatment. In this study, we performed comprehensive genetic and transcriptomic analyses of 16 pairs of primary-recurrent high-grade gliomas, a majority of those being glioblastomas. The data presented here show the presence of some well-described somatic mutations in genes such as *TP53*, *PTEN*, *PIK3R1*, *IDH1*, *ATRX*, and *PIK3CA* in HGGs. Somatic variants identified consistently in both primary and recurrent HGGs represent a small fraction of the total detected variants. This suggests that a large amount of somatic mutations identified in primary HGGs is not present at recurrence, which could be indicative of subclone substitution, where new subclones harbor different mutations, as suggested by another study [30] or by a neutral evolution and polyclonal re-emergence [32].

Loss of chr10 and amplification of chr7 are common aberrations in GBMs [8], and these aberrations were detected in our current CNA analysis. Profiles of CNAs were similar in primary and recurrent HGGs. Focusing on *EGFR* and *PTEN* CNAs, we found an inverse correlation between *EGFR* and *PTEN* focal aberrations (Fig. 2c, Suppl. Fig. S3), indicating a co-occurrence of these phenomena. *EGFR* amplification and deletion of *PTEN* produce similar consequences in deregulation of intracellular signaling activating pro-proliferative and pro-survival pathways [8].

From the genomic analysis performed in the GLASS study [36], a number of somatic variants specific to a primary or a recurrent tumor sample were higher than those shared between the two disease stages for most of the patients, which is in line with our results. Besides, their analysis of CNVs during the tumor's progression suggests that amplification of chromosome 7 and deletion of chromosome 10 are found in both early and later stages of the tumor evolution, notably in IDH-WT specimens [36]. The analysis of cancer driver genes in the GLASS cohort produced a set of genes consistent with our findings; in addition, we found *PIK3R1* as a potential cancer driver gene.

We found a novel frameshift insertion candidate in the *ZNF384* gene which might affect protein stability. The zinc finger protein 384 (ZNF384) is a transcription factor involved in the pathobiology of acute lymphoblastic leukemia through the *ZNF384* gene fusion with the *TET* family genes [37]. ZNF384 (also known as nuclear matrix protein 4 (NMP4)) has nucleocytoplasmic shuttling activity and suppresses bone anabolism, partially through the repression of genes that play important roles in osteogenic lineage commitment and mineralization [38]. In pre-osteoblasts, embryonic stem cells, and two blood cell lines, NMP4 binds to the promoters of genes encoding unfolded protein response (UPR) regulators and modulates their gene expression [38]. NMP4 may transcriptionally repress *c-Myc* and *Gadd34*, downregulating ribosome biogenesis and global protein synthesis [39]. Interestingly, high expression of *ZNF384* inversely correlated with survival (in TCGA-GBM/LGG dataset, Suppl. Fig. S1D).

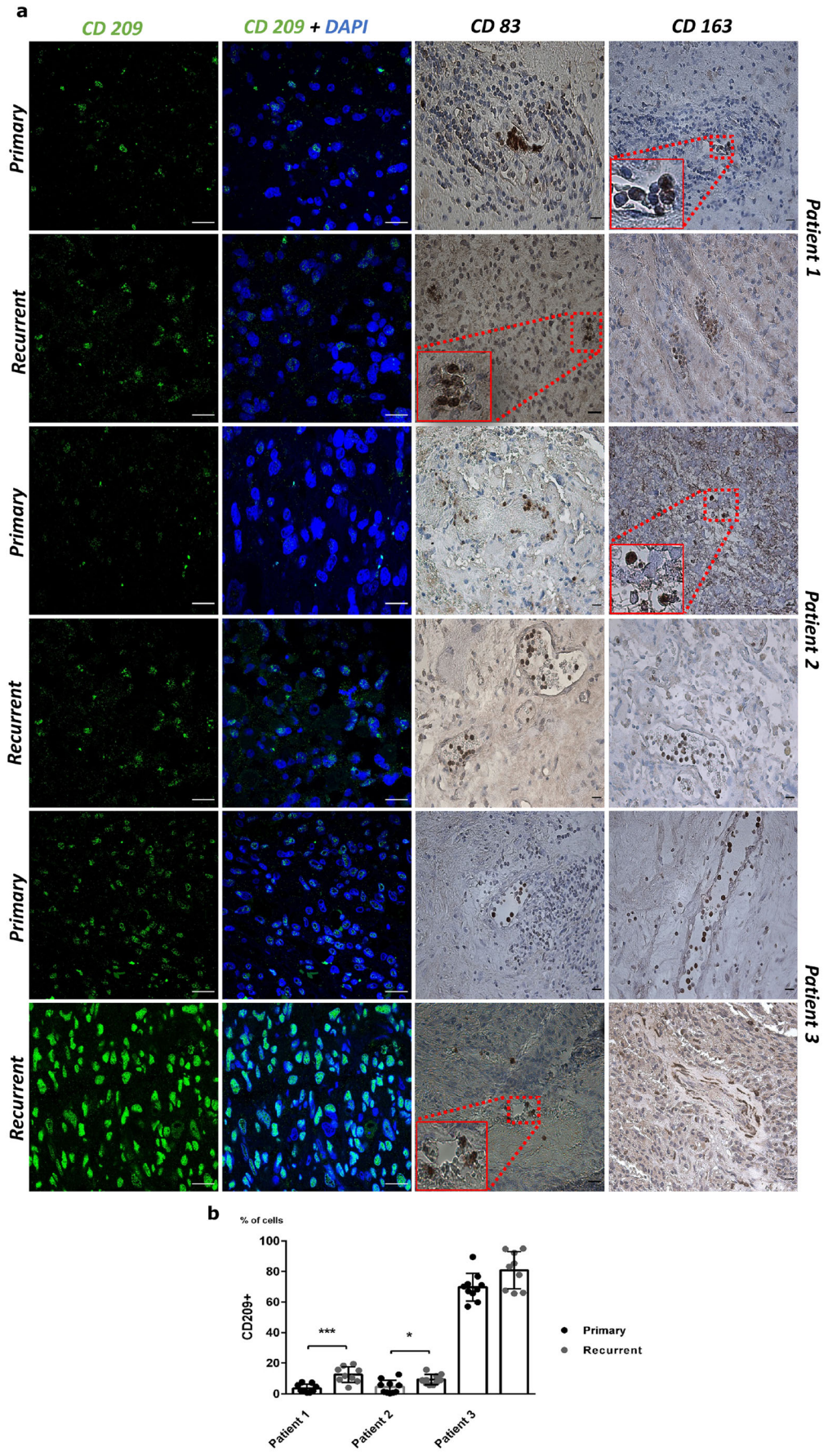
a
CD 209
CD 209 + DAPI
CD 83
CD 163
Primary
Recurrent
Primary
Recurrent
Primary
Recurrent
Patient 1
Patient 2
Patient 3
b
% of cells
CD209+
100
80
60
40
20
0
***
*
Patient 1
Patient 2
Patient 3
Primary
Recurrent

◀ **Fig. 5** Accumulation of pro-tumorigenic macrophages and immature dendritic cells in recurrent GBMs. **a** Representative confocal microscopy images show a higher number of immunosuppressive cells ($CD209^+$) in recurrent GBMs compared to primary GBMs; cell nuclei are counterstained with DAPI (blue) (scale bar 20 μm). Mature dendritic cells ($CD83^+$) and phagocytic microglia/macrophages ($CD163^+$) are shown. **b** Quantification of CD209-positive cells that were related to total cells. The cells were counted using ImageJ software from 10 fields, and the Mann–Whitney non-parametric test was used to compute *p* values

Transcriptomic analyses of HGGs at diagnosis and relapse showed downregulation of genes related to mRNA splicing, cell cycle, and DNA repair, with concomitant upregulation of genes related to interferon signaling. Deregulation of mRNA splicing, which was found in the pathway enrichment analysis (Fig. 3b, c), is consistent with differences in splicing isoforms between the tested groups (Fig. 3a). Abundance of splice variants and downregulation of genes coding for a splicing machinery suggests that spliceosome functions and mRNA processing are disrupted in recurrent HGGs. Cancer-specific splicing isoforms may be functionally distinct from the canonical isoforms found in normal tissues. As components of the splicing machinery are druggable, this deregulation could be exploited to improve clinical outcomes [40].

Further, functional analysis of differentially expressed genes demonstrated upregulation of IFN signaling–related genes. IFNs have anti-tumor [41] and anti-proliferative activity against glioblastoma cells [42], but autocrine IFN signaling contributes to the immune evasion of glioma cells [43]. Downregulation of numerous genes involved in the regulation of cell cycle and cell cycle checkpoints could be a consequence of IFN upregulation [42, 43]. Upregulation of mRNAs coding for components of PI signaling pathway (Fig. 3b) or PI metabolism (Fig. 3c) suggests a lipid second messenger deregulation in recurrent HGGs, which could result in an enhancement of cell migration and invasion.

Computational analysis of the immune microenvironment of HGGs during progression showed remarkable differences in the abundance of immune cells, mainly pro-tumorigenic (M2) macrophages, immature dendritic cells, and T helper cells. Dendritic cells are central regulators of the adaptive immune response, responsible for cancer recognition and eradication [44]. Activated, mature DCs are the main antigen-presenting cells for initiating adaptive immune responses, whereas immature DCs are implicated in tolerance and induction of regulatory T cells [45]. Antigen-presenting function of DCs is lost or inefficient in malignant gliomas [46]. Tumor-infiltrating DCs (TIDCs) may influence tumor progression, as seen in relapsed prostate cancer patients who had higher densities of immature TIDCs than their primary tumors [47]. Our results demonstrate an accumulation of immunosuppressive cells ($CD209^+$ cells) in recurrent HGGs that might disable anti-tumor responses and potentiate immunosuppression. The presence of a strong pro-tumorigenic macrophage signature and accumulation of phagocytic $CD163^+$ cells [48] in recurrent HGGs, which is partially in line with GLASS's in silico cell enrichment results [36], indicates the tumor supportive microenvironment and potentiation of immunosuppression post recurrence. These processes could be the main obstacles in effective glioma immunotherapy and must be overcome before introducing frontline immunotherapies in GBM.

Supplementary Information The online version contains supplementary material available at https://doi.org/10.1007/s00109-020-02005-7.

Acknowledgments We would like to thank the physicians who performed the surgeries, the patients for their consent for the use of their biological material for this research, and Dr. Chinchu Jayaprakash for improving the language quality of this manuscript.

Code availability Codes generated during the current study are available upon reasonable request.

Authors' contributions Design of the study, data analysis, data interpretation, and manuscript preparation were performed by Adria-Jaume Roura. RNA/DNA isolation, sequencing, and clinical table preparation were performed by Bartlomiej Gielniewski and Paulina Pilanc. Immunohistochemistry was carried out by Paulina Pilanc. Experimental design and preparation of the materials for experiments were performed by Marta Maleszweska and Sylwia K. Krol. Preparation of the clinical samples and collection of clinical information were performed by Ryszard Czepko and Wojciech Kaspera. Study design, data interpretation, and manuscript preparation were performed by Bartosz Wojtas and Bozena Kaminska. All authors read and approved the final manuscript.

Funding Studies were supported by the Foundation for Polish Science TEAM-TECH Core Facility project "NGS platform for comprehensive diagnostics and personalized therapy in neuro-oncology." The use of CePT infrastructure, financed by the European Union, The European Regional Development Fund within the Operational Programme "Innovative economy" for 2007–2013, is highly appreciated.

Data availability The data that support the findings of this study are openly available at the European Genome-phenome Archive (EGA), reference number EGAS00001004606.

Compliance with ethical standards

Conflict of interest The authors declare that they have no conflicts of interest.

Ethical approval This study was approved by the Bioethics Committees of St. Raphael Hospital, Andrzej Frycz Modrzewski Krakow University, Krakow, Poland (Nr. 73/KBL/OIL/2015); Medical University of Silesia, Sosnowiec, Poland; and Mazovian Brodno Hospital, Warsaw, Poland (Nr. KNW/0022/KB1/46/I/16), and have therefore been performed in accordance with the ethical standards laid down in the 1964 Declaration of Helsinki and its later amendments.

Consent to participate All persons gave their informed consent prior to their inclusion in the study. Details that might disclose the identity of the subjects under study have been omitted.

Consent for publication Not applicable.

References

1. Touat M, Idbaih A, Sanson M, Ligon KL (2017) Glioblastoma targeted therapy: updated approaches from recent biological insights. Ann Oncol 28:1457–1472
2. Verhaak RGW, Hoadley KA, Purdom E, Wang V, Qi Y, Wilkerson MD, Miller CR, Ding L, Golub T, Mesirov JP et al (2010) Integrated genomic analysis identifies clinically relevant subtypes of glioblastoma characterized by abnormalities in PDGFRA, IDH1, EGFR, and NF1. Cancer Cell 17:98–110
3. Brennan CW, Verhaak RGW, McKenna A, Campos B, Noushmehr H, Salama SR, Zheng S, Chakravarty D, Sanborn JZ, Berman SH et al (2013) The somatic genomic landscape of glioblastoma. Cell 155:462–477
4. Sturm D, Bender S, Jones DTW, Lichter P, Grill J, Becher O, Hawkins C, Majewski J, Jones C, Costello JF et al (2014) Paediatric and adult glioblastoma: multiform (epi)genomic culprits emerge. Nat Rev Cancer 14:92–107
5. An Z, Aksoy O, Zheng T, Fan Q-W, Weiss WA (2018) Epidermal growth factor receptor and EGFRvIII in glioblastoma: signaling pathways and targeted therapies. Oncogene 37:1561–1575
6. Kim H, Zheng S, Amini SS, Virk SM, Mikkelsen T, Brat DJ, Grimsby J, Sougnez C, Muller F, Hu J et al (2015) Whole-genome and multisector exome sequencing of primary and post-treatment glioblastoma reveals patterns of tumor evolution. Genome Res 25:316–327
7. Phillips HS, Kharbanda S, Chen R, Forrest WF, Soriano RH, Wu TD, Misra A, Nigro JM, Colman H, Soroceanu L et al (2006) Molecular subclasses of high-grade glioma predict prognosis, delineate a pattern of disease progression, and resemble stages in neurogenesis. Cancer Cell 9:157–173
8. Ceccarelli M, Barthel FP, Malta TM, Sabedot TS, Salama SR, Murray BA, Morozova O, Newton Y, Radenbaugh A, Pagnotta SM et al (2016) Molecular profiling reveals biologically discrete subsets and pathways of progression in diffuse glioma. Cell 164: 550–563
9. Perng P, Lim M (2015) Immunosuppressive mechanisms of malignant gliomas: parallels at non-CNS sites. Front Oncol 6:5
10. Ellert-Miklaszewska A, Dabrowski M, Lipko M, Sliwa M, Maleszewska M, Kaminska B (2013) Molecular definition of the pro-tumorigenic phenotype of glioma-activated microglia. Glia. 61: 1178–1190
11. Barthel FP, Johnson KC, Varn FS, Moskalik AD, Tanner G, Kocakavuk E, Anderson KJ, Abiola O, Aldape K, Alfaro KD et al (2019) Longitudinal molecular trajectories of diffuse glioma in adults. Nature 576:112–120
12. Gabrusiewicz K, Ellert-Miklaszewska A, Lipko M, Sielska M, Frankowska M, Kaminska B (2011) Characteristics of the alternative phenotype of microglia/macrophages and its modulation in experimental gliomas. PLoS One 6:e23902
13. Bolger AM, Lohse M, Usadel B (2014) Trimmomatic: a flexible trimmer for Illumina sequence data. Bioinformatics 30:2114–2120
14. Sedlazeck FJ, Rescheneder P, von Haeseler A (2013) NextGenMap: fast and accurate read mapping in highly polymorphic genomes. Bioinformatics 29:2790–2791
15. (2019) Picard Tools - By Broad Institute. Github.Io. broadinstitute.github.io/picard/
16. Koboldt DC, Zhang Q, Larson DE, Shen D, McLellan MD, Lin L, Miller CA, Mardis ER, Ding L, Wilson RK (2012) VarScan 2: somatic mutation and copy number alteration discovery in cancer by exome sequencing. Genome Res 22:568–576
17. Wang K, Li M, Hakonarson H (2010) ANNOVAR: functional annotation of genetic variants from high-throughput sequencing data. Nucleic Acids Res 38:e164–e164
18. Tamborero D, Gonzalez-Perez A, Lopez-Bigas N (2013) OncodriveCLUST: exploiting the positional clustering of somatic mutations to identify cancer genes. Bioinformatics 29:2238–2244
19. Wang L, Wang S, Li W (2012) RSeQC: quality control of RNA-seq experiments. Bioinformatics 28:2184–2185
20. Liao Y, Smyth GK, Shi W (2013) featureCounts: an efficient general purpose program for assigning sequence reads to genomic features. Bioinformatics 30:923–930
21. Dobin A, Davis CA, Schlesinger F, Drenkow J, Zaleski C, Jha S, Batut P, Chaisson M, Gingeras TR (2012) STAR: ultrafast universal RNA-seq aligner. Bioinformatics 29:15–21
22. Love MI, Huber W, Anders S (2014) Moderated estimation of fold change and dispersion for RNA-seq data with DESeq2. Genome Biology 15:550
23. Aran D, Hu Z, Butte AJ (2017) xCell: digitally portraying the tissue cellular heterogeneity landscape. Genome Biol 18:220
24. Becht E, Giraldo NA, Lacroix L, Buttard B, Elarouci N, Petitprez F, Selves J, Laurent-Puig P, Sautès-Fridman C, Fridman WH, et al (2016) Estimating the population abundance of tissue-infiltrating immune and stromal cell populations using gene expression. Genome Biol 17:218
25. Newman AM, Liu CL, Green MR, Gentles AJ, Feng W, Xu Y, Hoang CD, Diehn M, Alizadeh AA (2015) Robust enumeration of cell subsets from tissue expression profiles. Nat Methods 12(5): 453–457
26. Finotello F, Mayer C, Plattner C, Laschober G, Rieder D, Hackl H, Krogsdam A, Loncova Z, Posch W, Wilflingseder D, et al (2019) Molecular and pharmacological modulators of the tumor immune contexture revealed by deconvolution of RNA-seq data. Genome Med 11:34
27. Li B, Severson E, Pignon J-C, Zhao H, Li T, Novak J, Jiang P, Shen H, Aster JC, Rodig S, et al (2016) Comprehensive analyses of tumor immunity: implications for cancer immunotherapy. Genome Biol 17:174
28. Körber V, Yang J, Barah P, Wu Y, Stichel D, Gu Z, Fletcher MNC, Jones D, Hentschel B, Lamszus K et al (2019) Evolutionary trajectories of IDHWT glioblastomas reveal a common path of early tumorigenesis instigated years ahead of initial diagnosis. Cancer Cell 35:692–704.e12
29. Liu A, Hou C, Chen H, Zong X, Zong P (2016) Genetics and epigenetics of glioblastoma: applications and overall incidence of IDH1 mutation. Front Oncol 6:16
30. Wang J, Cazzato E, Ladewig E, Frattini V, Rosenbloom DIS, Zairis S, Abate F, Liu Z, Elliott O, Shin Y-J et al (2016) Clonal evolution of glioblastoma under therapy. Nat Genet 48:768–776
31. Gocho Y, Kiyokawa N, Ichikawa H, Nakabayashi K, Osumi T, Ishibashi T, Ueno H, Terada K, Oboki K, Sakamoto H et al (2015) A novel recurrent EP300–ZNF384 gene fusion in B-cell precursor acute lymphoblastic leukemia. Leukemia 29:2445–2448
32. Alexandrov LB, Nik-Zainal S, Wedge DC, Aparicio SAJR, Behjati S, Biankin AV, Bignell GR, Bolli N, Borg A, Børresen-Dale A-L et al (2013) Signatures of mutational processes in human cancer. Nature 500:415–421
33. Guo C, McDowell IC, Nodzenski M, Scholtens DM, Allen AS, Lowe WL, Reddy TE (2017) Transversions have larger regulatory effects than transitions. BMC Genomics 18:394
34. van Alphen RJ, Wiemer EAC, Burger H, Eskens FALM (2008) The spliceosome as target for anticancer treatment. Br J Cancer 100:228–232
35. Szulzewsky F, Pelz A, Feng X, Synowitz M, Markovic D, Langmann T, Holtman IR, Wang X, Eggen BJL, Boddeke HWGM et al (2015) Glioma-associated microglia/macrophages display an expression profile different from M1 and M2 polarization and highly express Gpnmb and Spp1. Harrison JK, editor. PLoS One 10:e0116644

36. Barthel FP, Johnson KC, Varn FS, Moskalik AD, Tanner G, Kocakavuk E, Anderson KJ, Abiola O, Aldape K, Alfaro KD et al (2019) Longitudinal molecular trajectories of diffuse glioma in adults. Nature 576(7785):112–120
37. Hirabayashi S, Ohki K, Nakabayashi K, Ichikawa H, Momozawa Y, Okamura K, Yaguchi A, Terada K, Saito Y, Yoshimi A et al (2016) ZNF384-related fusion genes define a subgroup of childhood B-cell precursor acute lymphoblastic leukemia with a characteristic immunotype. Haematologica 102:118–129
38. Childress P, Stayrook KR, Alvarez MB, Wang Z, Shao Y, Hernandez-Buquer S, Mack JK, Grese ZR, He Y, Horan D et al (2015) Genome-wide mapping and interrogation of the Nmp4 antianabolic bone axis. Mol Endocrinol 29:1269–1285
39. Young SK, Shao Y, Bidwell JP, Wek RC (2016) Nuclear matrix protein 4 is a novel regulator of ribosome biogenesis and controls the unfolded protein response via repression of Gadd34 expression. J Biol Chem 291:13780–13788
40. Danan-Gotthold M, Golan-Gerstl R, Eisenberg E, Meir K, Karni R, Levanon EY (2015) Identification of recurrent regulated alternative splicing events across human solid tumors. Nucleic Acids Res 43: 5130–5144
41. Yang CH, Wang Y, Sims M, Cai C, He P, Häcker H, Yue J, Cheng J, Boop FA, Pfeffer LM (2017) MicroRNA203a suppresses glioma tumorigenesis through an ATM-dependent interferon response pathway. Oncotarget 8:112980–112991
42. Tanabe T, Kominsky SL, Subramaniam PS, Johnson HM (2000) Torres BA. J. Neuro-Oncol 48:225–232
43. Silginer M, Nagy S, Happold C, Schneider H, Weller M, Roth P (2017) Autocrine activation of the IFN signaling pathway may promote immune escape in glioblastoma. Neuro-Oncol 19:1338–1349
44. Gardner A, Ruffell B (2016) Dendritic cells and cancer immunity. Trends Immunol 37:855–865
45. Kim R, Emi M, Tanabe K (2006) Functional roles of immature dendritic cells in impaired immunity of solid tumour and their targeted strategies for provoking tumour immunity. Clin Exp Immunol 146:189–196
46. Ma Y, Shurin GV, Peiyuan Z, Shurin MR (2013) Dendritic cells in the cancer microenvironment. J Cancer 4:36–44
47. Tran Janco JM, Lamichhane P, Karyampudi L, Knutson KL (2015) Tumor-infiltrating dendritic cells in cancer pathogenesis. J Immunol 194:2985–2991
48. Aras S, Zaidi MR (2017) TAMeless traitors: macrophages in cancer progression and metastasis. Br J Cancer 117:1583–1591